Optimizing the geometry of photoacoustically active gold nanoparticles for biomedical imaging

Article *in* ACS Photonics · January 2020

DOI: 10.1021/acsphotonics.9b01418

12 authors, including:

Rafaela Paz García Álvarez
The University of Manchester
4 PUBLICATIONS **82** CITATIONS
SEE PROFILE

Alexander Nedilko
RWTH Aachen University
3 PUBLICATIONS **16** CITATIONS
SEE PROFILE

Anne Rix
RWTH Aachen University
43 PUBLICATIONS **484** CITATIONS
SEE PROFILE

Vertika Pathak
RWTH Aachen University
5 PUBLICATIONS **112** CITATIONS
SEE PROFILE

ACS Photonics

pubs.acs.org/journal/apchd5

Article

Optimizing the Geometry of Photoacoustically Active Gold Nanoparticles for Biomedical Imaging

Rafaela García-Álvarez, Lisa Chen, Alexander Nedilko, Ana Sánchez-Iglesias, Anne Rix, Wiltrud Lederle, Vertika Pathak, Twan Lammers, Gero von Plessen, Kostas Kostarelos, Luis M. Liz-Marzán, Alexander J. C. Kuehne,* and Dmitry N. Chigrin*

Cite This: https://dx.doi.org/10.1021/acsphotonics.9b01418

ABSTRACT: Photoacoustics is an upcoming modality for biomedical imaging, which promises minimal invasiveness at high penetration depths of several centimeters. For superior photoacoustic contrast, imaging probes with high photothermal conversion efficiency are required. Gold nanoparticles are among the best performing photoacoustic imaging probes. However, the geometry and size of the nanoparticles determine their photothermal efficiency. We present a systematic theoretical analysis to determine the optimum nanoparticle geometry with respect to photoacoustic efficiency in the near-infrared spectral range, for superior photoacoustic contrast. Theoretical predictions are illustrated by experimental results for two of the most promising nanoparticle geometries, namely, high aspect ratio gold nanorods and gold nanostars.

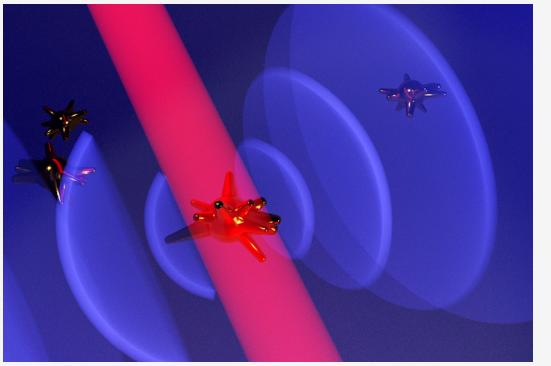

KEYWORDS: *photoacoustics, gold nanoparticles, biomedical imaging, theoretical modeling, plasmon resonance*

Gold nanoparticles represent a versatile class of materials, with potential application in various fields, including photoacoustic imaging.[1−3] Pulsed excitation of plasmonic gold nanoparticles leads to periodic heating and thermal expansion and contraction of the particle, as well as the surrounding medium, which can be recorded as ultrasound waves using a conventional ultrasound transducer.[4] For biomedical imaging, photoacoustics is advantageous over fluorescence imaging, as only the excitation light beam needs to penetrate through the tissue.[5] Light becomes attenuated due to absorption and scattering by biological structures, while ultrasound waves can travel through tissue almost unhindered. Tissue exhibits the least absorption and background scattering in the near-infrared region, from about 700 to 1300 nm, which is why this spectral region is commonly described as the tissue transparency window.[6] Depending on the shape and size of the plasmonic gold particles, the attenuation can be spectrally shifted into the desired examination window, to gain information also from deep underneath the skin.[3]

A wide variety of synthetic strategies have been developed to obtain gold nanoparticle shapes in a controlled fashion, ranging from spheres, shells, bipyramids, and rods, to cages and stars.[7,8] Edges and tips present in some geometries lead to the enhancement of the electromagnetic field in these tapers and the emergence of hotspots, where the plasmon-polaritons relax thermally (via electron−phonon coupling).[9] However, different shapes also exhibit different ratios between absorption and scattering, which may limit the applicability of such gold nanostructures in photoacoustic imaging.[10,11] To date, mainly gold nanorods, nanocages, and nanoshells have been applied for biomedical photoacoustic imaging.[12−17] However, the complete parameter space of nanoparticle size, length, diameter, and other degrees of freedom with respect to their optimal photoacoustic performance have not been optimized and the contributions of the individual factors are not well understood. This lack of understanding leads to the use of unsuitable or underperforming gold nanoparticle architectures and limited photoacoustic contrast in imaging applications.

Here, we identify the most important parameters for plasmonic nanoparticle design, enabling identification of the optimal gold nanoparticle shape and size for maximized photoacoustic efficiency within the tissue transparency window. While the optimal structure is probably impossible to obtain, we approach this ideal by developing suitable size and shape ranges for gold nanorods and gold nanostars. We compare their actual photoacoustic performance with model simulations.

Received: September 30, 2019
Published: January 23, 2020

The photoacoustic intensity generated by a small plasmonic nanoparticle as part of an ensemble can be described using a point source model.[13,18] In this case, the intensity from a single nanoparticle is proportional to its absorption cross-section σ_a and the fluence of the laser radiation Φ at the source location x

$$s_{PA}(x) \propto \sigma_a \Phi(x) \propto \sigma_a \frac{W(x)}{S} \tag{1}$$

Here, $W(x)$ is the power of the laser radiation and S is the laser beam cross section area. In analyzing the total photoacoustic intensity, one has to consider that the laser radiation is attenuated as it passes through the sample (see Figure 1a). Using the Beer–Lambert law

$$W(x) = W_0 \exp\left(-\sigma_e \frac{N}{V} x\right) \tag{2}$$

the photoacoustic intensity from the thin layer dx at position x can be estimated as

$$s_{PA}(x)\frac{N}{V}S\mathrm{d}x \propto \sigma_a W_0 \exp\left(-\sigma_e \frac{N}{V} x\right)\frac{N}{V}\mathrm{d}x \tag{3}$$

Here, W_0 is the power of the laser at the sample entrance, σ_e is the extinction cross-section of the nanoparticle, N is the total number of nanoparticles in the illuminated volume V, and N/V is the nanoparticle density. After integration over the sample length L, the total photoacoustic intensity, S_{PA}, is given by

$$S_{PA} \propto W_0 \frac{\sigma_a}{\sigma_e}\left(1 - \exp\left(-\frac{\sigma_e L}{m} c\right)\right) \tag{4}$$

Here, the weight concentration of nanoparticles c has been introduced

$$c = m\frac{N}{V} \tag{5}$$

m being the mass of a single particle.

The total photoacoustic intensity is plotted in Figure 1b,c as a function of nanoparticle concentration, for different absorption and extinction cross sections. It can be seen that two distinct regimes exist. For small concentrations ($\frac{\sigma_e L}{m} c \ll 1$), the total photoacoustic intensity is linearly dependent on the concentration and the absorption cross-section

$$S_{PA} \propto W_0 L \frac{\sigma_a}{m} c = \alpha c \tag{6}$$

where α is the photoacoustic efficiency at low concentrations. In order to maximize the photoacoustic efficiency for low concentrations, the absorption cross-section has to be maximized. For large concentrations ($\frac{\sigma_e L}{m} c \gg 1$), the total photoacoustic intensity saturates toward a constant value

$$S_{PA} \propto \frac{\sigma_a}{\sigma_e} \tag{7}$$

To maximize the photoacoustic efficiency in this case, the absorption cross-section has to be maximized with respect to the extinction cross-section. These observations allow to formulate a first design principle for achieving high performance of the photoacoustic point source: (i) the absorption cross-section of the nanoparticle has to be maximized, not only with respect to its absolute value, but also with respect to the extinction cross-section. Therefore, an ideal photoacoustic probe should display maximal absorption and minimal scattering efficiencies.

For small nanoparticles, the absorption cross-section is proportional to the imaginary part of the particle polarizability α, $\sigma_a \sim \mathrm{Im}\alpha$. The scattering cross-section, σ_s, is proportional to the absolute value squared of the polarizability, $\sigma_s \sim |\alpha|^2$. The polarizability itself is proportional to the particle volume v. Therefore, the absorption cross-section of a plasmonic nanoparticle scales with the particle volume, while its scattering cross-section does with the volume squared, v^2. This results in the dominance of absorption over scattering for the particles with a small volume.[19] Unfortunately, this effect is accompanied by a shift of the plasmon resonance toward the plasma frequency, and so away from the near-infrared (NIR) transparency window of biological tissue. It is well-known that the plasmon resonance frequency can be shifted toward longer wavelengths by elongating the particle geometry.[19] Combining this with the requirement that the particle volume must be kept small, one arrives at the second design rule for achieving optimal performance of the nanoparticle photoacoustic source: (ii) the nanoparticle volume has to be kept small with simultaneous increase of one nanoparticle dimension. This requirement can be satisfied by using small nanoparticles with a large aspect ratio.

Obvious candidates for an optimal photoacoustic source are long, high-aspect ratio nanorods or nanowires.[20] We thus calculated the absolute absorption cross-section and relative

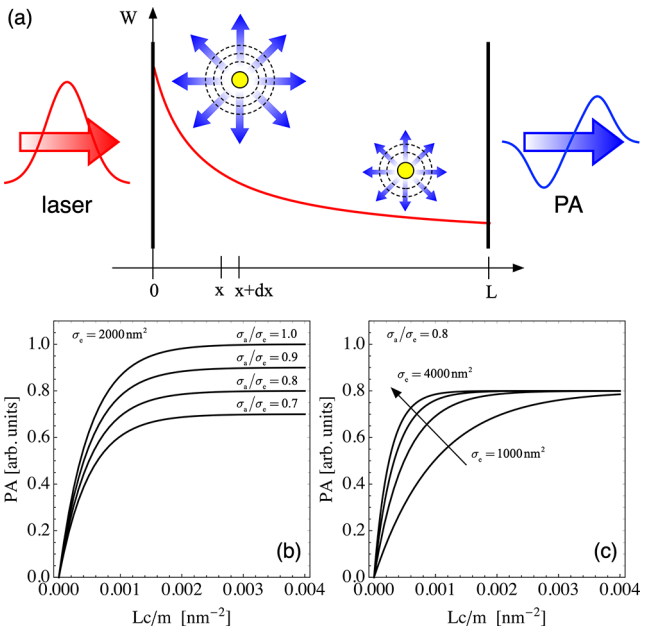

Figure 1. (a) A sketch of photoacoustic (PA) intensity recording. Gold nanoparticles are heated by an incident laser radiation and generate an ultrasound signal. The intensity of the laser beam drops as it propagates through the sample. (b) Photoacoustic intensity normalized to incident power, as given by eq 4, for different fractions of absorption in the extinction cross-sections (70–100%). The extinction cross-section is assumed to be equal to σ_e = 2000 nm^2. (c) Photoacoustic intensity for different extinction cross sections, from σ_e = 1000 nm^2 to σ_e = 4000 nm^2. The fraction of absorption in the extinction cross sections is 80%. With increasing concentration, the photoacoustic intensity increases linearly at low concentrations, while at high particle concentrations, the intensity saturates.

https://dx.doi.org/10.1021/acsphotonics.9b01418
ACS Photonics XXXX, XXX, XXX−XXX

absorption of gold nanorods at their absorption maxima, for different diameters and lengths (different aspect ratios), as a function of a corresponding wavelength (Figure 2). Relative

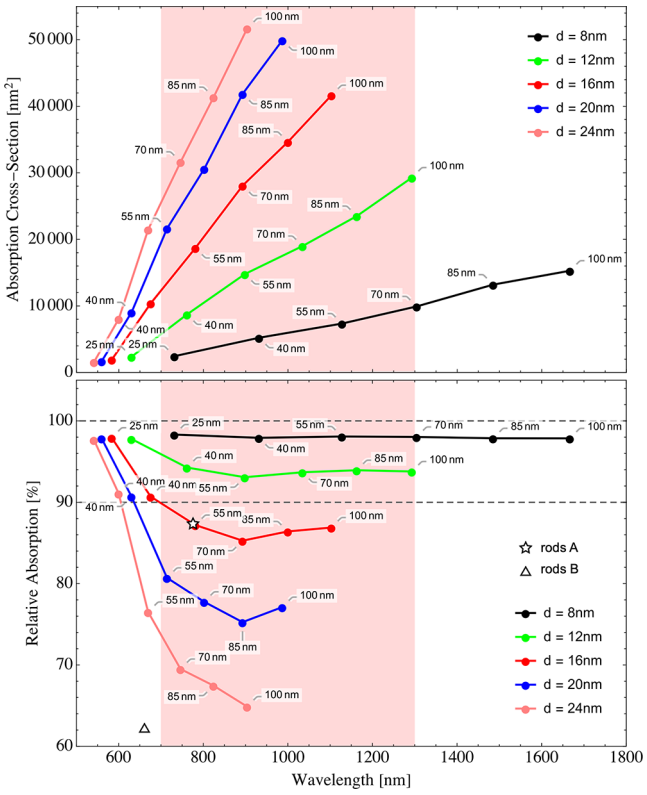

Figure 2. Absolute absorption cross-section (top) and relative absorption (bottom) of gold nanorods at their respective absorption maxima, as a function of the corresponding wavelength. Results for different nanorod diameters (d) and lengths (noted near the corresponding points) are shown. The light red area marks the NIR transparency window of biological tissue.

absorption is defined as the ratio of the absorption to extinction cross sections, σ_a/σ_e. All calculations were performed using a commercial solver, CST Studio Suite. We employed a finite element solver with the plane-wave excitation linearly polarized along the long axis of the nanorod, in combination with far-field monitors. Open boundary conditions were used to simulate an infinite water background. Water was assumed to have a refractive index of 1.33. The Johnson-Christy values were used for the wavelength-dependent dielectric function of gold.[21] It can be clearly seen that an increase in the nanorod length leads to a shift of the resonance toward longer wavelengths (Figure 2). An increase of the nanoparticle volume results in the simultaneous increase of the absolute absorption and reduction of the relative absorption. A reasonable compromise between the two trends is achieved for nanorods with diameter d = 12 nm and length between l = 40 nm and l = 100 nm. These nanorods demonstrate both large absolute and relative absorption in the NIR transparency window of biological tissue (Figure 2). However, such high aspect ratio gold nanorods have been reported to suffer from degradation due to Rayleigh instability,[22,23] that is, breakage of high aspect ratio gold nanostructures into smaller pieces over time. This degradation is accompanied by a shift of the resonant absorption band toward the visible spectral range, considerably reducing the NIR absorption efficiency over time.

A compromise between long-term stability of the nanoparticle and high absorption efficiency in the NIR spectral range is offered by gold nanostars.[24] Nanostars consist of a small quasi-spherical core (typical diameter 10−25 nm) and many sharp tips (typical length: 5−25 nm). Their plasmonic response can be roughly understood by considering hybridization of particle plasmon polaritons of the core and the high aspect ratio nanorods representing nanostar tips.[25] Due to the large spectral separation between the corresponding plasmon polariton resonances, the NIR absorption efficiency of gold nanostars resembles that of high aspect ratio gold nanorods, demonstrating both large absolute and relative absorption.[26] We calculated the absolute absorption cross-section and relative absorption at the absorption maximum wavelength for different nanostar geometries, as shown in Figure 3. Three

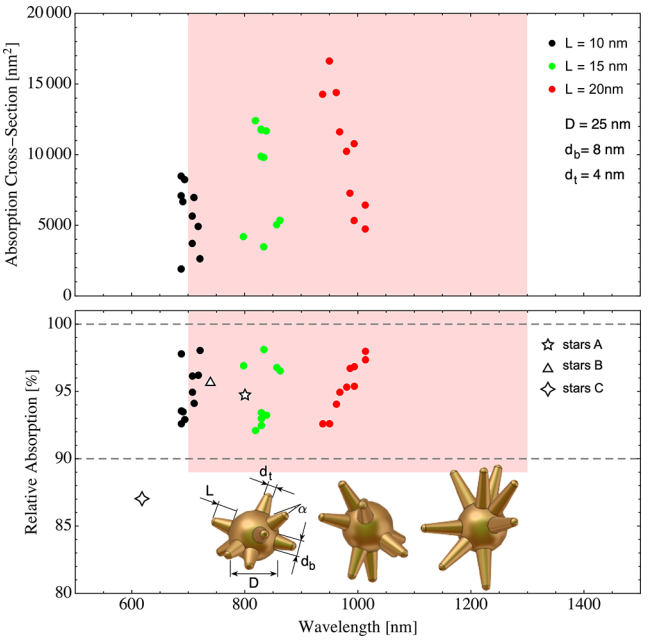

Figure 3. Absolute absorption cross-section (top) and relative absorption (bottom) of gold nanostars at their respective absorption maxima, as a function of the corresponding wavelength. Results for different nanostar geometries are shown. Representations of the geometries with relevant dimensions are provided as insets. The light red area marks the NIR transparency window of biological tissue.

geometries were considered. They all had a core diameter of D = 25 nm and diameter of the tip base and tip top of d_b = 8 nm and d_t = 4 nm, respectively. Results for 10 random realizations for tip lengths L = 10, 15, and 25 nm are shown. Every realization differs by number and placement of the tips, with an average number of tips $\langle N \rangle$ = 10 and a standard deviation σ_N = 4. For all nanostar geometries, both absolute and relative absorption are high and comparable with those of long aspect ratio nanorods. Nanostars with tip lengths larger than L = 10 nm satisfy both conditions for an optimal photoacoustic probe, as defined above.

In order to confirm our theoretical predictions, we determined the attenuation (extinction), absorption and scattering coefficients of dispersions of gold nanorods and nanostars, with geometries fulfilling the conditions for optimal photoacoustic performance. Gold nanorods with average length of 38.0 ± 3.8 nm and diameter of 10.0 ± 1.0 nm were used. The rods were stabilized by cetyltrimethylammo-

https://dx.doi.org/10.1021/acsphotonics.9b01418
ACS Photonics XXXX, XXX, XXX−XXX

nium bromide (CTAB) and dispersed in water. Gold nanostars were synthesized following previously reported protocols.[27−29] Geometrical parameters of the nanostars were determined through inspection of at least 100 particles in TEM images. The average equivalent diameter of the nanostars was 45.0 ± 5.0 nm, with an average core diameter of 25.0 ± 2.0 nm. Experimental attenuation, absorption and scattering coefficients are shown for nanorods and nanostars in Figure 4a and b, respectively. The measurements were performed by using an integrating sphere setup. The setup consists of an Andor spectrometer (iDus 420 CCD camera and Shamrock 303i spectrograph) and an integrating sphere with barium sulfate coating (UPB-150-ARTA from Gigahertz-Optik). Both nanoparticle types demonstrated pronounced resonances in the NIR transparency window near 750 nm, with absorption dominating over scattering. The resonance band of nanostars was found to be largely broadened, compared to nanorod resonances, due to higher dispersity in nanostar geometries. Both nanoparticle types show high relative absorption at the maximum absorption wavelength, with 87.3% and 95.7% for nanorods and nanostars, respectively.

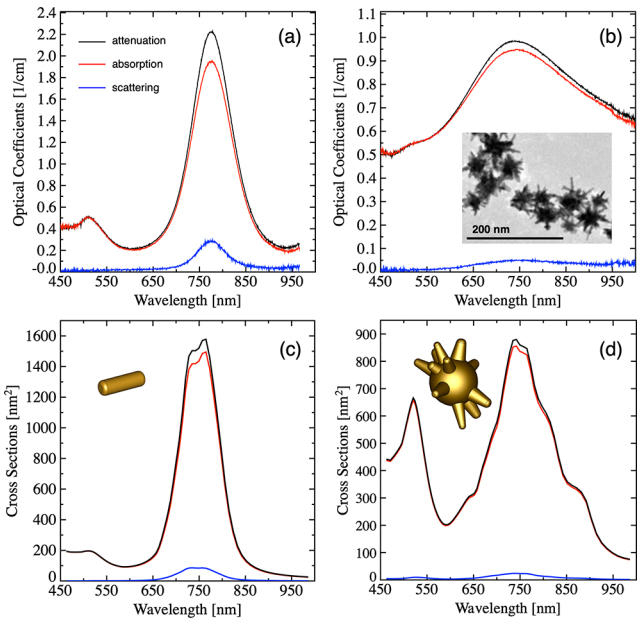

Figure 4. Top panel: Experimental attenuation (extinction), absorption, and scattering coefficients for nanorods (a) and nanostars (b). Inset shows a representative TEM image of nanostars. Relative absorption at the absorption maximum is 87.3% and 95.7% for nanorods and nanostars, respectively. Measurements were performed for different concentrations of nanorods and nanostars. Bottom panel: Theoretical extinction, absorption and scattering cross-sections for gold nanorods (c) and gold nanostars (d). All theoretical spectra were averaged over 100 random realizations of the corresponding geometries. Insets show representative examples of simulated structures. Relative absorption values at the absorption maxima are 94.5% and 97.1% for nanorods and nanostars, respectively.

Calculated attenuation, absorption, and scattering cross sections for gold nanorods and gold nanostars are shown in Figure 4c and d, respectively. All spectra were calculated for linearly polarized plane wave excitation and averaged over 100 realizations of randomly oriented nanorods (c) and nanostars (d) geometries. The best fit to the experimental data was obtained for nanorods with average length $\langle L \rangle$ = 38.0 nm, standard deviation of σ_L = 2 nm and average diameter $\langle d \rangle$ = 12.0 nm nm with σ_d = 1.0 nm. For nanostars, the best fit was obtained for a core diameter of 25 nm, average number of tips of $\langle N \rangle$ = 6, with σ_N = 4, length of tips $\langle L \rangle$ = 10.0 nm, with σ_L = 2.0 nm, diameter of the tip at the top of $\langle d_t \rangle$ = 4.0 nm, with σ_{d_t} = 1.0 nm and taper opening angle of $\langle \alpha \rangle$ = 8.0° with σ_α = 2°. The calculated spectral position of the plasmon resonances, as well as the relative and absolute absorption values, are in good agreement with the experimental data. Both types of nanoparticles demonstrated large relative and absolute absorption efficiencies, with relative absorption at maximum wavelength being 94.5% and 97.1% for nanorods and nanostars, respectively.

Experimentally determined relative absorption at the respective absorption maxima of several nanorods and nanostars are summarized in Figure 2, bottom, and Figure 3, bottom. Two types of nanorods are analyzed. Relative absorption of the type-A (type-B) nanorods with an average length of 38.0 ± 3.8 nm (71.0 ± 2.0 nm) and a diameter of 10.0 ± 1.0 nm (25.0 ± 1.0 nm) is shown as a star (triangle) in Figure 2, bottom. Relative absorption of three types of gold nanostars, with the average equivalent diameter of 55.0 ± 5.0 nm (type-A), 45.0 ± 5.0 nm (type-B), and 35.0 ± 5.0 nm (type-C) are depicted in Figure 3, bottom, as star, triangle, and diamond, respectively. For all types of nanostars, the average core diameter is estimated to be 25.0 ± 2.0 nm. Overall, these data are in good agreement with the numerical predictions and further support the proposed design rules: high aspect ratio nanoparticles with small overall volume are preferable for optimal absorption efficiency.

We thus proceeded to investigate the photoacoustic intensity for optimized nanorod and nanostar geometries. For comparison, we also include the results for a nonoptimized plasmonic nanostructure, namely, nanospheres of a comparable diameter (d = 44 nm), as shown in Figure 5. We calculated the theoretical photoacoustic intensity using eq 4 and the absorption and extinction cross sections reported in Figure 4c,d for gold nanorods and nanostars (Figure 5a,c). For gold nanospheres we determined the attenuation cross section by averaging over 100 realizations, with an average diameter of 44 nm and a standard deviation of 6 nm (not shown here). The length of the sample was assumed to be 600 μm, which corresponds to the length of the experimentally used phantom. The numerical value of the laser power at different wavelengths was obtained from the literature.[30] The average mass of the gold nanoparticles was calculated using their averaged volume and density (ρ = 19300 kg/m^3).[31] The photoacoustic intensity from both nanorods and nanostars was found to follow the spectral shape of the attenuation cross section, being considerably stronger than the intensity from gold nanospheres across all excitation wavelengths and concentrations (Figure 5a,c). For a concentration of c = 0.4 g/L, the intensity enhancement was as large as 55 and 35 times for nanorods and nanostars, respectively (see Figure 5a). The dependence of the total photoacoustic intensity as a function of concentration, calculated as a sum over the wavelength interval from 690 to 900 nm, shows the expected and characteristic saturation behavior (compare with Figure 1b,c). While the absorption cross section for gold nanorods is larger than that for nanostars, the photoacoustic intensity from nanorods grows faster for low concentrations, but also saturates at lower values due to the smaller relative absorption.

https://dx.doi.org/10.1021/acsphotonics.9b01418
ACS Photonics XXXX, XXX, XXX−XXX

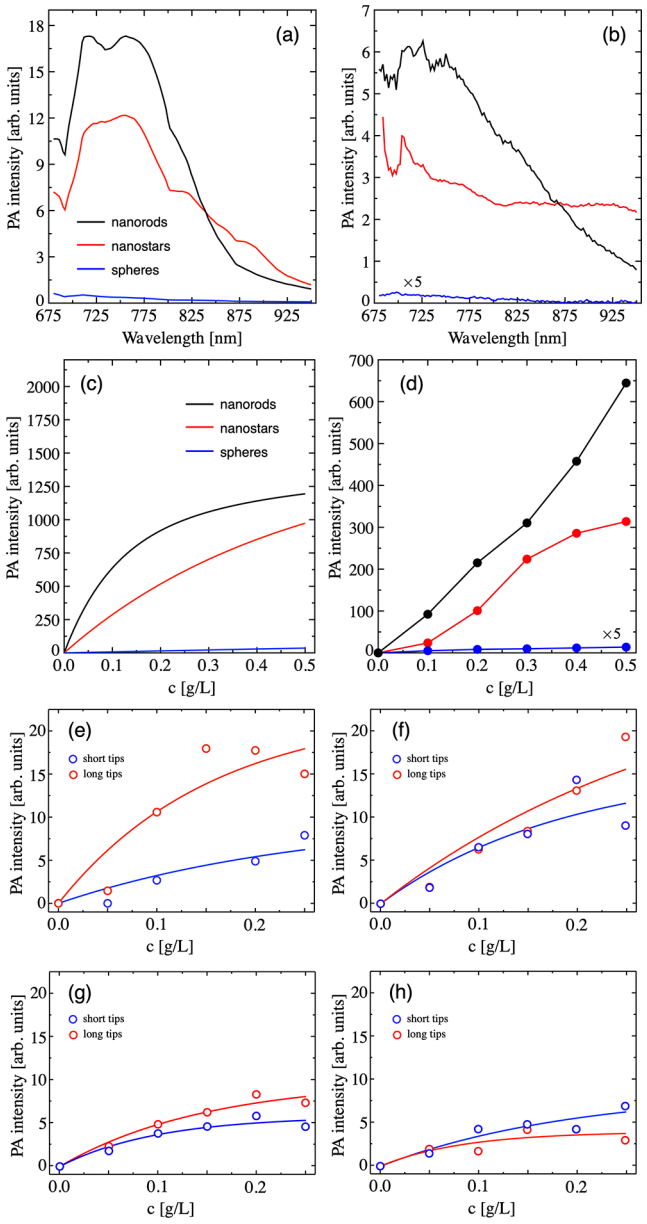

Figure 5. (a, b) Photoacoustic intensity as a function of excitation laser wavelength. Theoretical (a) and experimental (b) data are shown for a concentration c = 0.4 g/L. (c, d) Theoretical (c) and experimental (d) total photoacoustic intensities over a wavelength range from 690 to 900 nm as a function of concentration. Data for nanorods (black), nanostars (red), and nanospheres (blue) are shown. Experimental photoacoustic intensity for nanospheres is multiplied by a factor of 5. (e–h) Photoacoustic intensity vs concentration for eight different types of gold nanostars. Nanostars with 30 (e), 40 (f), 50 (g), and 60 nm (h) cores each with short and long tips are shown. Circles are for measured data and curves are for fits to eq 4.

Photoacoustic measurements of synthesized[27−29] nanorods, nanostars, and nanospheres were performed on a Visualsonics Vevo LAZR or an LED-based photoacoustic system from PreXion Corporation. The gold nanoparticles were analyzed in tubing phantoms (air bubble free polyurethane intravascular tubing, 0.025 × 0.040 in, INSTECH) as an aqueous dispersion of the corresponding nanoparticle concentration. The previously described gold nanorods, nanostars and nanospheres were used. The spectral dependence of the photoacoustic intensity showed good qualitative agreement with the theoretical prediction (Figure 5b). For a concentration of c = 0.4 g/L (Figure 5a), the intensity enhancement with respect to the intensity from nanospheres is as large as 35- and 25-fold for nanorods and nanostars, respectively. The concentration dependence of the photoacoustic intensity showed the expected saturation character in the case of nanostars (Figure 5d). However, for gold nanorods the photoacoustic intensity deviated substantially from the expected trend for large concentrations (c > 0.4 g/L). We attribute this behavior to additional nonlinearities of the photoacoustic process, which are not considered by our model. To further showcase the suitability of our design rules, we synthesized and analyzed eight different types of gold nanostars. They are based on four seeds with diameters of 30, 40, 50, and 60 nm and possess short (avg 12 nm) as well as long tips (avg 17 nm). The concentration-dependent photoacoustic intensity upon excitation with a 750 nm LED (30 mW/cm^2) is shown in Figure 5e,f. Experimental data are successfully fitted to the analytical expression (eq 4), demonstrating suitability of the developed model. In accordance with the predictions, gold nanostars with smaller volume and longer tips outperform nanostars with larger volume and shorter tips as a photoacoustic source.

In conclusion, we have developed a theoretical model for the photoacoustic response of gold nanoparticles, considering their size, tip length, and taper angle, as well as batch heterogeneity. This model allows to formulate two simple constraints for nanoparticle properties, to obtain an optimal photoacoustic performance in the tissue transparency window. We demonstrate that gold nanorods and nanostars can be designed to fulfill both constraints. While gold nanorods exhibit slightly better performance, their biocompatibility and cytotoxicity might limit their application.[9] Gold nanostars might represent the superior geometry with comparable performance and better biocompatibility. However, previous studies have shown that biocompatibility can be improved by coating the gold nanoparticles with inert materials.[13] In the future, the here developed model will allow modeling the performance of gold nanoparticles for a variety of further applications. Furthermore, the model represents a means to derive guidelines for the development of other nanoparticle shapes and materials for photoacoustic imaging applications.

AUTHOR INFORMATION

Corresponding Authors

Alexander J. C. Kuehne − *DWI − Leibniz Institute for Interactive Materials, 52076 Aachen, Germany; Institute of Organic and Macromolecular Chemistry, Ulm University, 89081 Ulm, Germany;* orcid.org/0000-0003-0142-8001; Email: alexander.kuehne@uni-ulm.de

Dmitry N. Chigrin − *DWI − Leibniz Institute for Interactive Materials, 52076 Aachen, Germany; I. Physikalisches Institut (1A), RWTH Aachen University, 52056 Aachen, Germany;* orcid.org/0000-0002-8197-707X; Email: chigrin@dwi.rwth-aachen.de

Authors

Rafaela García-Álvarez − *DWI − Leibniz Institute for Interactive Materials, 52076 Aachen, Germany; CIC biomaGUNE and Ciber-BBN, Basque Research and Technology Alliance (BRTA), 20014 Donostia-San Sebastián, Spain; Nanomedicine Lab, Faculty of Biology, Medicine and*

https://dx.doi.org/10.1021/acsphotonics.9b01418
ACS Photonics XXXX, XXX, XXX−XXX

Health, and National Graphene Institute, The University of Manchester, Manchester M13 9PT, United Kingdom

Lisa Chen − *DWI − Leibniz Institute for Interactive Materials, 52076 Aachen, Germany; Institute of Organic and Macromolecular Chemistry, Ulm University, 89081 Ulm, Germany*

Alexander Nedilko − *I. Physikalisches Institut (1A), RWTH Aachen University, 52056 Aachen, Germany*

Ana Sánchez-Iglesias − *CIC biomaGUNE and Ciber-BBN, Basque Research and Technology Alliance (BRTA), 20014 Donostia-San Sebastián, Spain*

Anne Rix − *Institute for Experimental Molecular Imaging, Medical Faculty, RWTH Aachen University, 52074 Aachen, Germany*

Wiltrud Lederle − *Institute for Experimental Molecular Imaging, Medical Faculty, RWTH Aachen University, 52074 Aachen, Germany*

Vertika Pathak − *Institute for Experimental Molecular Imaging, Medical Faculty, RWTH Aachen University, 52074 Aachen, Germany*

Twan Lammers − *Institute for Experimental Molecular Imaging, Medical Faculty, RWTH Aachen University, 52074 Aachen, Germany;* orcid.org/0000-0002-1090-6805

Gero von Plessen − *I. Physikalisches Institut (1A), RWTH Aachen University, 52056 Aachen, Germany*

Kostas Kostarelos − *Nanomedicine Lab, Faculty of Biology, Medicine and Health, and National Graphene Institute, The University of Manchester, Manchester M13 9PT, United Kingdom;* orcid.org/0000-0002-2224-6672

Luis M. Liz-Marzán − *CIC biomaGUNE and Ciber-BBN, Basque Research and Technology Alliance (BRTA), 20014 Donostia-San Sebastián, Spain; Ikerbasque, Basque Foundation for Science, 48013 Bilbao, Spain;* orcid.org/0000-0002-6647-1353

Complete contact information is available at: https://pubs.acs.org/10.1021/acsphotonics.9b01418

Author Contributions

A.J.C.K., L.L.-M., and D.N.C. devised the idea for this study. R.G.-Á. performed gold nanoparticle synthesis, spectral analysis, and photoacoustic experiments. A.S.I. helped with the nanoparticle synthesis. A.R., L.C., W.L., and T.L. gave access and assisted in the photoacoustic experiments. A.N. and G.v.P. performed high resolution spectroscopy. D.N.C. developed the theoretical model and performed the numerical calculations. A.J.C.K. and D.N.C. wrote the first draft and all authors contributed in revising the manuscript to the current form.

Notes

The authors declare no competing financial interest.

■ ACKNOWLEDGMENTS

The authors acknowledge financial support from the European Commission (EUSMI, 731019 and from the DFG (German Science Foundation) through the collaborative research center SFB 985 "Functional Microgels and Microgel Systems" in Project A7. L.M.L.M. acknowledges funding from the Spanish MINECO (Grant MAT2017-86659-R) and the Maria de Maeztu Units of Excellence Program from the Spanish State Research Agency, Grant No. MDM-2017-0720. D.N.C. acknowledges a partial support by the DFG through the Heisenberg Fellowship (CH 407/7-2).

■ REFERENCES

(1) Li, W.; Chen, X. Gold Nanoparticles for Photoacoustic Imaging. *Nanomedicine* **2015**, *10*, 299−320.

(2) Cox, B.; Laufer, J. G.; Arridge, S. R.; Beard, P. C. Quantitative Spectroscopic Photoacoustic Imaging: A Review. *J. Biomed. Opt.* **2012**, *17*, 061202.

(3) Dreaden, E. C.; Alkilany, A. M.; Huang, X.; Murphy, C. J.; El-Sayed, M. a. The Golden Age: Gold Nanoparticles for Biomedicine. *Chem. Soc. Rev.* **2012**, *41*, 2740.

(4) Xu, M.; Wang, L. V. Photoacoustic Imaging in Biomedicine. *Rev. Sci. Instrum.* **2006**, *77*, 041101.

(5) Mallidi, S.; Luke, G. P.; Emelianov, S. Photoacoustic Imaging in Cancer Detection, Diagnosis, and Treatment Guidance. *Trends Biotechnol.* **2011**, *29*, 213−221.

(6) Pansare, V. J.; Hejazi, S.; Faenza, W. J.; Prud'Homme, R. K. Review of Long-Wavelength Optical and NIR Imaging Materials: Contrast Agents, Fluorophores, and Multifunctional Nano Carriers. *Chem. Mater.* **2012**, *24*, 812−827.

(7) Grzelczak, M.; Pérez-Juste, J.; Mulvaney, P.; Liz-Marzán, L. M. Shape Control in Gold Nanoparticle Synthesis. *Chem. Soc. Rev.* **2008**, *37*, 1783−1791.

(8) Hu, M.; Chen, J.; Li, Z. Y.; Au, L.; Hartland, G. V.; Li, X.; Marquez, M.; Xia, Y. Gold Nanostructures: Engineering Their Plasmonic Properties for Biomedical Applications. *Chem. Soc. Rev.* **2006**, *35*, 1084−1094.

(9) Wang, Y.; Black, K. C. L.; Luehmann, H.; Li, W.; Zhang, Y.; Cai, X.; Wan, D.; Liu, S. Y.; Li, M.; Kim, P.; et al. Comparison Study of Gold Nanohexapods, Nanorods, and Nanocages for Photothermal Cancer Treatment. *ACS Nano* **2013**, *7*, 2068−2077.

(10) Jauffred, L.; Samadi, A.; Klingberg, H.; Bendix, P. M.; Oddershede, L. B. Plasmonic Heating of Nanostructures. *Chem. Rev.* **2019**, *119*, 8087.

(11) Jain, P. K.; Lee, K. S.; El-Sayed, I. H.; El-Sayed, M. A. Calculated Absorption and Scattering Properties of Gold Nanoparticles of Different Size, Shape, and Composition: Applications in Biological Imaging and Biomedicine. *J. Phys. Chem. B* **2006**, *110*, 7238−7248.

(12) Wu, D.; Huang, L.; Jiang, M. S.; Jiang, H. Contrast Agents for Photoacoustic and Thermoacoustic Imaging: A Review. *Int. J. Mol. Sci.* **2014**, *15*, 23616−23639.

(13) Repenko, T.; Rix, A.; Nedilko, A.; Rose, J.; Hermann, A.; Vinokur, R.; Moli, S.; Cao-Milàn, R.; Mayer, M.; Plessen von, G.; et al. Strong Photoacoustic Signal Enhancement by Coating Gold Nanoparticles with Melanin for Biomedical Imaging. *Adv. Funct. Mater.* **2018**, *28*, 1705607.

(14) Wilson, K.; Homan, K.; Emelianov, S. Biomedical Photoacoustics beyond Thermal Expansion Using Triggered Nanodroplet Vaporization for Contrast-Enhanced Imaging. *Nat. Commun.* **2012**, *3*, 610−618.

(15) Jokerst, J. V.; Cole, A. J.; Van De Sompel, D.; Gambhir, S. S. Gold Nanorods for Ovarian Cancer Detection with Photoacoustic Imaging and Resection Guidance via Raman Imaging in Living Mice. *ACS Nano* **2012**, *6*, 10366−10377.

(16) Wang, Y.; Xie, X.; Wang, X.; Ku, G.; Gill, K. L.; O'Neal, D. P.; Stoica, G.; Wang, L. V. Photoacoustic Tomography of a Nanoshell Contrast Agent in the in Vivo Rat Brain. *Nano Lett.* **2004**, *4*, 1689−1692.

(17) Yang, X.; Skrabalak, S. E.; Li, Z. Y.; Xia, Y.; Wang, L. V. Photoacoustic Tomography of a Rat Cerebral Cortex in Vivo with Au Nanocages as an Optical Contrast Agent. *Nano Lett.* **2007**, *7*, 3798−3802.

(18) Xu, M.; Wang, L. V. Photoacoustic Imaging in Biomedicine. *Rev. Sci. Instrum.* **2006**, *77*, 041101.

(19) Novotny, L.; Hecht, B. *Principles of Nano-Optics*; Cambridge University Press, 2012.

(20) Pazos-Perez, N.; Baranov, D.; Irsen, S.; Hilgendorff, M.; Liz-Marzan, L. M.; Giersig, M. Synthesis of Flexible, Ultrathin Gold Nanowires in Organic Media. *Langmuir* **2008**, *24*, 9855−9860.

(21) Johnson, P. B.; Christy, R. W. Optical Constants of the Noble Metals. *Phys. Rev. B* **1972**, *6*, 4370−4379.
(22) Xu, S.; Li, P.; Lu, Y. In Situ Atomic-Scale Analysis of Rayleigh Instability in Ultrathin Gold Nanowires. *Nano Res.* **2018**, *11*, 625−632.
(23) Karim, S.; Toimil-Molares, M. E.; Balogh, A. G.; Ensinger, W.; Cornelius, T. W.; Khan, E. U.; Neumann, R. Morphological Evolution of Au Nanowires Controlled by Rayleigh Instability. *Nanotechnology* **2006**, *17*, 5954−5959.
(24) Guerrero-Martínez, A.; Barbosa, S.; Pastoriza-Santos, I.; Liz-Marzán, L. M. Nanostars Shine Bright for You. Colloidal Synthesis, Properties and Applications of Branched Metallic Nanoparticles. *Curr. Opin. Colloid Interface Sci.* **2011**, *16*, 118−127.
(25) Hao, F.; Nehl, C. L.; Hafner, J. H.; Nordlander, P. Plasmon Resonances of a Gold Nanostar. *Nano Lett.* **2007**, *7*, 729−732.
(26) Yuan, H.; Khoury, C. G.; Wilson, C. M.; Grant, G. A.; Bennett, A. J.; Vo-Dinh, T. In Vivo Particle Tracking and Photothermal Ablation Using Plasmon-Resonant Gold Nanostars. *Nanomedicine* **2012**, *8*, 1355−1363.
(27) Pérez-Juste, J.; Pastoriza-Santos, I.; Liz-Marzán, L. M.; Mulvaney, P. Gold Nanorods: Synthesis, Characterization and Applications. *Coord. Chem. Rev.* **2005**, *249*, 1870−1901.
(28) Kumar, P. S.; Pastoriza-Santos, I.; Rodriguez-Gonzalez, B.; Garcia de Abajo, F. J.; Liz-Marzan, L. M. High-Yield Synthesis and Optical Response of Gold Nanostars. *Nanotechnology* **2008**, *19*, 015606.
(29) Barbosa, S.; Agrawal, A.; Rodríguez-Lorenzo, L.; Pastoriza-Santos, I.; Alvarez-Puebla, R. A.; Kornowski, A.; Weller, H.; Liz-Marzán, L. M. Tuning Size and Sensing Properties in Colloidal Gold Nanostars. *Langmuir* **2010**, *26*, 14943−14950.
(30) Bohndiek, S. E.; Bodapati, S.; Van De Sompel, D.; Kothapalli, S. R.; Gambhir, S. S. Development and Application of Stable Phantoms for the Evaluation of Photoacoustic Imaging Instruments. *PLoS One* **2013**, *8*, 1−14.
(31) Cengel, Y. A.; Biles, M. A. *Thermodynamics: An Engineering Approach*, 8th ed.; McGraw-Hill Education, 2014.

https://dx.doi.org/10.1021/acsphotonics.9b01418
ACS Photonics XXXX, XXX, XXX−XXX